Journal of Power Sources 196 (2011) 4769–4778

Contents lists available at ScienceDirect

Journal of Power Sources

journal homepage: www.elsevier.com/locate/jpowsour

Current density and state of charge inhomogeneities in Li-ion battery cells with $LiFePO_4$ as cathode material due to temperature gradients☆

Matthias Fleckenstein[a,*], Oliver Bohlen[a], Michael A. Roscher[b], Bernard Bäker[c]

[a] BMW Group, 80788 Munich, Germany
[b] RWTH Aachen University, Institute for Power Electronics and Electrical Drives ISEA, 52066 Aachen, Germany
[c] Dresden University of Technology, Department of Vehicle Mechatronics, Institute of Automotive Engineering, 01069 Dresden, Germany

ARTICLE INFO

Article history:
Received 22 September 2010
Received in revised form 10 January 2011
Accepted 16 January 2011
Available online 26 January 2011

Keywords:
Temperature distribution
Spatial thermal electrical cell simulation
Battery cooling
Open circuit voltage hysteresis

ABSTRACT

Current density distributions and local state of charge (SoC) differences that are caused by temperature gradients inside actively cooled Li-ion battery cells are discussed and quantified. As an example, a cylindrical Li-ion cell with $LiFePO_4$ as cathode material ($LiFePO_4$-cell) is analyzed in detail both experimentally and by means of spatial electro-thermal co-simulations. The reason for current density inhomogeneities is found to be the local electrochemical impedance varying with temperature in different regions of the jelly roll. For the investigated cell, high power cycling and the resulting temperature gradient additionally cause SoC-gradients inside the jelly roll. The local SoCs inside one cell diverge firstly because of asymmetric current density distributions during charge and discharge inside the cell and secondly because of the temperature dependence of the local open circuit potential. Even after long relaxation periods, the SoC distribution in cycled $LiFePO_4$-cells remains inhomogeneous across the jelly roll as a result of hysteresis in the open circuit voltage. The occurring thermal electrical inhomogeneities are expected to influence local aging differences and thus, global cell aging. Additionally the occurrence of inhomogeneous current flow and SoC-development inside non-uniformly cooled battery packs of parallel connected $LiFePO_4$-cells is measured and discussed.

1. Introduction

According to literature the most important impact factors on calendar life aging of Li-ion-cells are temperature and SoC [1–3], the main influencing factors on cycle life are temperature, current density, depth of discharge per cycle (ΔDoD), and SoC [1,3–5]. Generally, the electrochemical aging effects lead to an increase in cell impedance and a loss of cell capacity. Recently, Liu et al. [6] reported that the aging progress of $LiFePO_4$/graphite systems that are also investigated in this work is dominated by the loss of active lithium and, thus, induces mainly the loss of capacity with only little changes in the cell impedance. The data of capacity loss presented in that article show also a dependency on temperature and current rate for cycled $LiFePO_4$/graphite systems. Most cycle life models (e.g. [4,5]) consider global values of one or more cell states and cycling conditions, such as temperature, current density and SoC [1–5]. This approach neglects thermal and electric inhomogeneities inside the cell; the impact of temperature gradients and the resulting current density and SoC gradients across the cell's jelly roll is not considered. The methods and results presented in this article contribute to a better understanding of macroscopic electric and thermal interactions during cycling, which are influenced by the cell design and the cooling design outside the cell. It is beyond the scope of this article to parameterize a spatialized aging model for $LiFePO_4$ batteries. However, to reproduce the effects that mainly influence the aging processes (namely current, state of charge, and temperature) a thermal–electric cell model with spatial resolution is introduced in this work. Thus temperature gradients, current density distributions, and gradients of SoC inside a battery cell during cycling can be simulated. This detailed cell simulation is of high interest for interpreting electric and aging behavior of Li-ion cells, which are not only influenced by the maximum temperature of the cell but also by the temperature distribution occurring inside electrode stacks. This novel approach provides a valuable tool for examining the temperature spread inside battery cells and modules for system design.

☆ Parts of this article have previously been published at: 2nd Technical Conference "Advanced Battery Technologies for Automobiles and Their Electric Power Grid Integration" in Mainz/Germany (2010/02).

* Corresponding author at: BMW Group, Hufelandstraße 4-8a, 80788 München, Germany. Tel.: +49 89 382 14063; fax: +49 89 382 7014063.
E-mail address: Matthias.Fleckenstein@bmw.de (M. Fleckenstein).

0378-7753/$ – see front matter © 2011 Elsevier B.V. All rights reserved.
doi:10.1016/j.jpowsour.2011.01.043

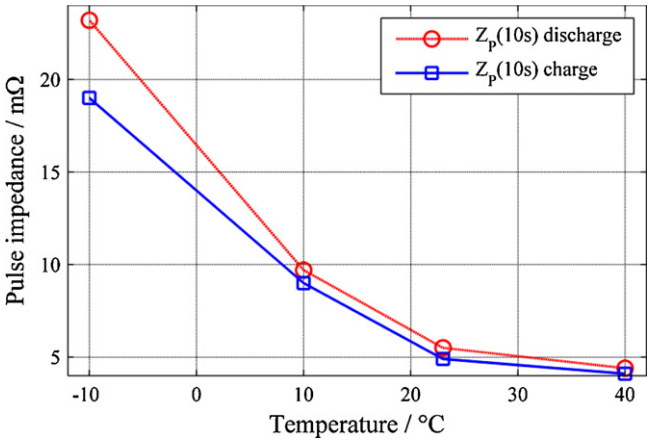

Fig. 1. Pulse impedance $Z_P(10\,s)$ of the investigated $LiFePO_4$-cell after 10 s of high current pulses for discharge and charge loads (88 A).

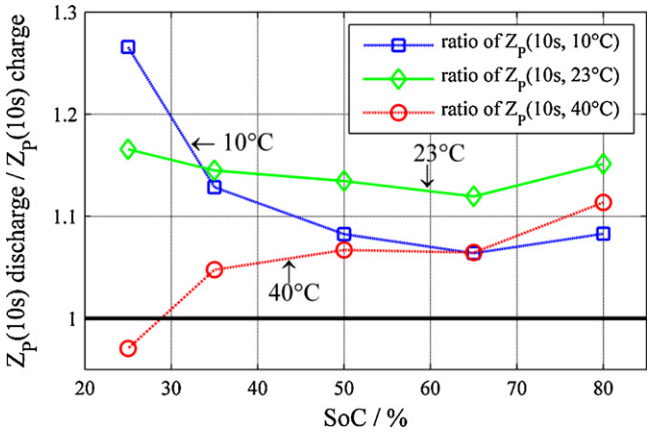

Fig. 2. Ratio of 10 s-discharge pulse impedance to 10 s-charge pulse impedance for the investigated $LiFePO_4$-cell dependent on temperature and SoC.

2. Theoretical background

For a better understanding of cell state inhomogeneities, first the macroscopic thermal–electric effects that are expected to occur inside the jelly roll of a Li-ion cell during operation should be highlighted. In this section the theoretical background is described qualitatively without using simulative results. A validated thermal–electric simulation model reproducing these effects is introduced in Section 3. All figures in this section that contain values of electric cell performance are based on measurements on the cylindrical $LiFePO_4$ cell used in the experimental section. Its electric and thermal characteristics can be seen in Table 1.

2.1. Temperature gradient

During cycling Li-ion cells generate heat mainly in consequence of overpotential under current load (irreversible heat) and changes in entropy (reversible heat). This thermal energy heats up the cell and, as cell temperature exceeds ambient temperature, it is conducted to the cell surface, where it is dissipated into the environment. As a result a gradient in temperature from the warmer inner elements of the jelly roll to the colder outer elements occurs inside the cell [7]. The simulative description of heat generation and of the occurring temperature distribution inside the cell is declared in Section 3.

2.2. Gradient of current density and heat generation

In order to compare the electric behavior of a Li-ion cell for different temperatures in the time domain the term pulse impedance $Z_p(t)$ is used. It describes the cell's normalized overvoltage response on constant current steps in dependence on time.

$$Z_p(t) = \frac{\Delta U(t)}{\Delta I(t)} \quad (1)$$

Fig. 1 shows the measured values of Z_p after 10 s pulse load for the investigated cell as a function of temperature. All values depend on measurements at a starting SoC of 50%.

Considering the thermal–electric interdependencies, we can assume that warmer regions of a Li-ion cell comprise lower electric impedance than colder cell regions and—as the regions are electrically connected in parallel to the colder cell regions—exhibit higher current densities during operation. Because of the quadratic dependency of local ohmic power loss on current density, the heat generation in different cell regions will grow with temperature. As a result we expect a higher temperature gradient occurring in real Li-ion cells compared to the results of thermal and electric cell-models that disregard the influence of electric and thermal interactions in spatially extended systems.

2.3. Gradient in SoC

In the following it is demonstrated that, beside a current density distribution, a SoC-difference inside a $LiFePO_4$-cell is expected to occur as a result of temperature gradients even after SoC-neutral current load profiles. In this article two effects will be discussed as possible reasons for SoC inhomogeneities:

1) The varying ratio of charge/discharge impedance.
2) The temperature dependency of OCV.

2.3.1. SoC-differences caused by varying ratio of charge/discharge impedance

As we can see in Fig. 1, the pulse impedance varies with temperature and differs for charge and discharge loads. Fig. 2 shows that additionally the ratio of discharge to charge pulse impedance varies for the investigated $LiFePO_4$ cells against temperature. In Fig. 2 the ratio of the 10 s-discharge pulse impedance to the 10 s-charge pulse impedance, the $Z_P(10\,s)$-ratio, is plotted against SoC at three different temperatures (10, 23 and 40 °C).

For temperatures between 23 °C and 40 °C the ratio of discharge to charge pulse impedance decreases with increasing temperature. In contrast, for lower temperatures (23–10 °C) the ratio increases with increasing temperature (except for 25% SoC). These qualitative curves were found for the ratio of the 30 s pulse impedance as well. An explicit electrochemical reason for this behavior is not yet found as the ratio is influenced by numerous causes and as the ratio's maxima vs. temperature seems to be the result of at least two counteracting thermodynamical effects. However, the discussion of the experiments will show a good agreement of the measured ratios for the observed temperature range between 23 and 40 °C with the cells' behavior in the experimental results.

In the case of a cycled cell with temperature gradient inside, different cell regions comprise different magnitudes of discharge to charge impedance unbalances. As a consequence, current density distributions inside the jelly roll during charge and discharge will differ. For a long-lasting current cycle with several charge and discharge periods these unbalances in current distribution can be considered as a time-averaged superposed current flow from one cell region to another. In the case of a cell operated with temperature gradient between 23 °C and 40 °C the colder cell regions of the $LiFePO_4$-cell possess larger relative discharge impedance and thus will be less discharged during discharge mode than charged

Table 1
Thermal and electrical cell specifications of the investigated Li-ion cell.

Cathode material	$LiFePO_4$	Can material	Aluminum
Anode material	Graphite	Jelly roll length	100 mm
Nominal voltage	3.3 V	Jelly roll density	2680 kg m^{-3}
Nominal capacity	4.4 Ah	Jelly roll heat capacity	950 J kg K^{-1}
Geometrical cell type	Cylindrical	Jelly roll thermal conductivity (axial, tangential)	0.4 W mK^{-1}
Cell housing diameter	32 mm	Jelly roll thermal conductivity (radial)	76 W mK^{-1}
Cell housing length	113 mm		

during charge mode. Consequently, even during SoC-neutral cycles, the local SoC-values inside the $LiFePO_4$-cell diverge. This effect (charge drift effect 1, CDE 1) is limited by the growing OCV difference caused by the non-uniform SoC distribution in the cell. As a result, the SoC drift should converge to a limited value depending on the charge and discharge current rates of the load profile. At other temperature ranges of increasing Z_P-ratio with increasing temperature (below 23 °C), this effect results in a SoC-difference in reversed direction.

2.3.2. SoC-differences caused by the temperature dependency of OCV

The second effect discussed in this article as a reason for drifting SoC is the dependency of open circuit potential on temperature, which can be seen in Fig. 3 for the investigated $LiFePO_4$-cell. Here, voltage profiles were monitored for cells under open-circuit conditions during variation of the ambient temperature between −20 and 40 °C. These measurements were done at different SoCs reached after charge, or after discharge periods. Comparing the cells' surface temperature profile to the voltage profile, the linear temperature coefficient of OCV (dU_0/dT) was determined. For 50% SoC, the positive temperature coefficient rises up to 0.12 mV K^{-1}. Similar values for $LiFePO_4$/graphite-cells can be found in literature [8]. The shape and the maxima of the dU_0/dT curve against SoC correspond with the entropy change measurements of Viswanathan et al. [9]. As the $LiFePO_4$-electrode seems to exhibit only small changes in entropy with varying SoC, the graphite electrode can be identified as the main influence on the dU_0/dT characteristics. According to Yazami and Reynier [10], entropy change-peaks against SoC can be explained by phase-transitions during lithium-ion intercalation in graphite at explicit concentrations of lithium atoms in Li_xC_6 [10,11].

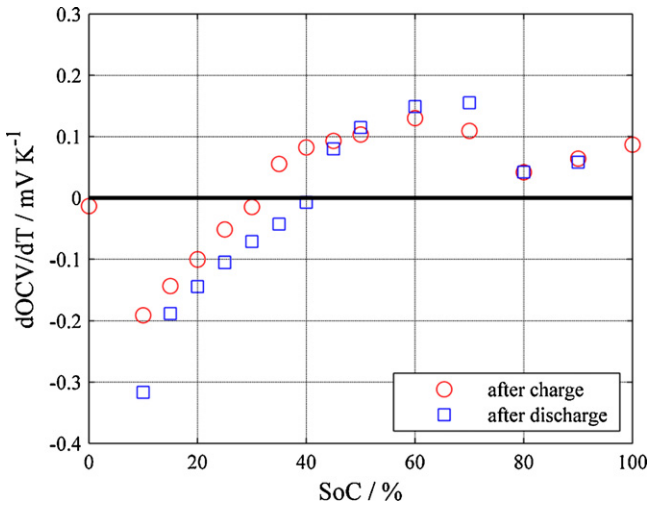

Fig. 3. Linear temperature coefficient of OCV vs. SoC of the investigated $LiFePO_4$-cell.

Transferred to the given problem of an inhomogenously tempered cell, warmer cell elements reach higher OCV-values than the colder elements of the cell assuming the same SoC. In consequence of this potential difference between the cell regions, a superposed transfer current occurs discharging the warmer cell elements with higher OCV and charging the colder elements. The current flow remains until the open circuit potential difference is equalized. The integrated transfer current equates the fraction of SoC drift caused by temperature dependent OCV. Thus, the effect of growing OCV against temperature (CDE 2) also leads to a gradient of SoC across the elements from the colder and higher charged elements to the warmer and lower charged elements.

2.3.3. Behavior of SoC-difference during relaxation periods

In order to interpret the occurrence and decay of SoC-differences during relaxation periods the characteristics of the open circuit voltage has to be known. In the first case we assume a single-valued OCV-characteristic against SoC (Fig. 4, left). This means, that the OCV of a cell would be identical after charge and discharge loads for the same SoC and temperature. Thus, it would not be dependent on the load history. After a high current load period the arisen SoC drift should be eliminated directly after cycling (CDE 1) or during temperature equalization (CDE 2), respectively, by transfer currents between the elements due to potential differences (ΔOCV in Fig. 4). After longer rest periods the SoC difference would completely vanish. This is schematically depicted in Fig. 4 (left). The SoCs of two elements in a cell—different in SoC after cycling (A and B)—assimilate in potential and thus run along the OCV-curve towards each other to the same threshold (C). No difference in SoC would persist. This assumption is a good approximation for electrode chemistries which show an OCV-hysteresis (see below) that is small compared to the gradient $dU_0/dSoC$.

Li-ion cells with $LiFePO_4$-cathodes comprise a distinct OCV hysteresis. This effect is characterized in several publications (e.g. [12]) and can be seen as the coexistence of two OCV-characteristics, after charge and after discharge loads in consequence of varying Li-ion concentrations on the electrode surfaces. For the given scenario – relaxation period right after high power cycling – a transfer current would occur similar to the case of a unique OCV-characteristic degrading the SoC-difference. If a higher charge throughput (ΔSoC >10%) had been operated right before the end of cycling, all elements would be located in the OCV-SoC diagram close to the upper border of the hysteresis area (A and B in Fig. 4 right).

During relaxation for the two observed elements in Fig. 4 (right), the element with lower SoC (A) is further charged by the transfer current in consequence of the voltage difference. As a result the element runs upwards the upper OCV curve (C'). The element with higher SoC (B) sees a change in the current direction at the end of cycling and gets discharged during relaxation. On the OCV-SoC diagram the point of element B moves in the direction of the lower OCV curve, the discharge OCV-curve (C″). The transfer current persists until all elements have reached the same OCV. Considering the non unique SoC-OCV characteristic a SoC difference remains even after complete compensation of the element temperatures (ΔSoC_∞). This hysteresis effect influences the charge balancing after discharge pulses in an analog way.

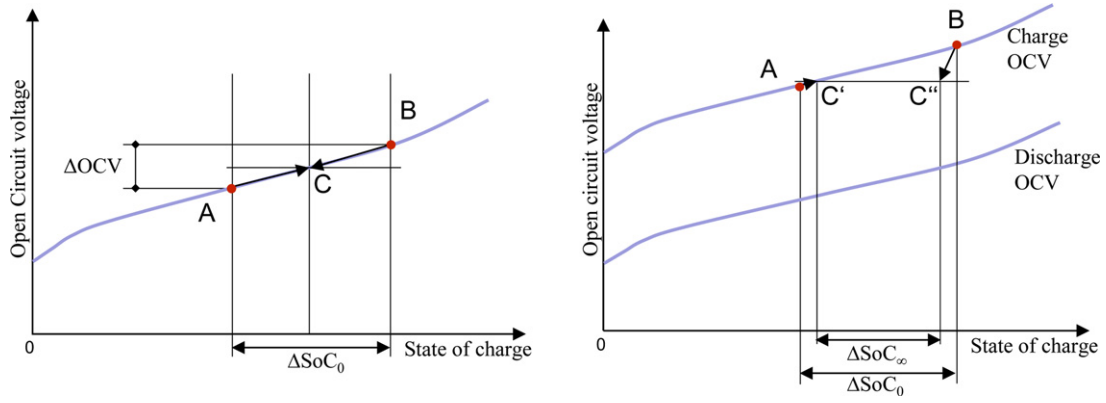

Fig. 4. Behavior of the local OCV of a high charged (A) and a low charged (B) jelly roll element during relaxation in a schematic OCV-SoC-diagram, left: considering a unique OCV-SoC characteristic, resulting in a single SoC-equalization (C); right: considering a OCV hysteresis in dependency on current direction. The OCV of B runs during relaxation to point C". The original SoC-difference (ΔSoC_0) is reduced to a constant SoC-difference (ΔSoC_∞). For further explanation see Section 2.3.3.

3. Simulation model

It is well-known, that the interdependencies between thermal and electrochemical behavior of a battery-cell make a permanent co-simulation of an electric and a thermal model mandatory to predict the cell's behavior precisely. This was considered by Gu and Wang [13], who coupled the volume-averaged thermal energy equation with a first-principle electrochemical model. This model uses the heat generation and the temperature-dependent physiochemical properties of transport, kinetics and mass-transfer as interfaces between thermal and electric model. Later Srinivasan and Wang [14] extended a similar model with a thermal 2D-model including the local heat generation method.

The following thermal–electric simulation model of the cylindrical $LiFePO_4$-cell was used to reproduce the experimental part and on the other hand in the later discussion to quantify thermal–electric inhomogeneities inside a single $LiFePO_4$-cell during operation. Therefore, local thermal and electrical distributions inside the cell had to be calculable. Thus, a spatially resolved three dimensional thermal model in combination with an impedance based spatially resolved three dimensional electric model of the cell's jelly roll is used for simulation. The time-discrete model was implemented using the simulation software Matlab Simulink [15]. Detailed information on the two submodels is given in the following, and was also reported previously in [16].

3.1. Thermal model

The correlation of heat flux and temperature development inside the jelly roll depends on the phenomenon of heat conductivity and is described by Fourier's law of heat conduction [17]. Considering the cell's geometry, it is applied for cylindrical coordinates:

$$\frac{\lambda}{\rho c}\nabla^2 T + \frac{\dot{q}_q}{\rho c} = \frac{\delta T}{\delta t} \quad \text{with} \quad \nabla^2 T = \frac{1}{r}\frac{\delta}{\delta r}\left(r\frac{\delta T}{\delta r}\right) + \frac{1}{r^2}\frac{\delta^2 T}{\delta \varphi^2} + \frac{\delta^2}{\delta z^2} \tag{2}$$

Abbreviations and parameter definitions of all equations are given in Table A1.

The jelly roll, consisting of a spirally wound electrode stack, is macroscopically modeled as a homogenous hollow cylinder with anisotropic heat conduction properties – exhibiting a low radial and a high axial and tangential thermal conductivity. The differential equation of heat conduction is discretizised with the finite-volume-method (FVM) that is applied for three dimensions in cylindrical coordinates (7 volume elements in radial direction, 5 in axial direction, 4 in tangential direction). Thus, the discretization divides the jelly roll in 140 discret elements of the same volume. The temperature of each volume element (VE) is calculated by thermal energy conservation considering reversible and irreversible heat sources of each VE and interacting heat fluxes between the adjoining VEs. The explicit numeric solution of the differential equation for one VE in order to calculate the temperatures for the next time step out of the given temperature distribution is given in Eq. (3).

$$T_E(t+\Delta t) = T_E(t) + \frac{1}{\rho V_E c}\left(\sum_{i=1}^{n}\frac{T_i(t)-T_E(t)}{R_{th,E,i}} + \dot{Q}_{irr,E} + \dot{Q}_{rev,E}\right)\Delta t \tag{3}$$

Subscript E (for element) indicates a VE specific value (temperature or heat source). Subscript n indicates the number of adjoining VEs, T_i is the temperature of the ith adjoining VE and $R_{th,E,i}$ is the thermal resistance from VE E to the ith adjoining VE. R_{th} is a geometry dependent value influenced by thermal conductivity. The thermal conductivity and the specific heat capacity of the homogenous jelly roll are assumed to be constant in the investigated temperature range and independent of SoC.

Irreversible and reversible heat generation for each control volume is mathematically implemented in the cell simulations according to Wu et al. [18]:

$$\dot{Q}_{irr} = \sum_{i=1}^{n} R_{i,E} \times I_{i,E}^2 \tag{4}$$

$$\dot{Q}_{rev} = T_E \frac{dU_{0,E}}{dT} \times I_E \tag{5}$$

R_i indicates the ith ohmic resistance of a user-defined equivalent circuit model (ECM) with n ohmic resistances inside the element E. $I_{i,E}$ indicates the current flow through $R_{i,E}$. $U_{0,E}$ is the open circuit voltage of element E and an approximation for the thermodynamic equilibrium voltage that can be seen as the threshold of the OCV for infinitely long resting periods. I_E is the current flow through the serial elements of the used local ECM in element E. The heat generation effect by heat of mixing and parasitic chemical reactions, as discussed in [18,19], do play a minor role in overall heat generation during operation and are neglected.

The cell peripherals – anode and cathode terminals and housing – were modeled as a network of thermal capacities and resistances. The thermal resistances of free convection on the cell housings' surface are considered by a global heat transfer coefficient α on cells surface. The values of α were determined in previous experiments.

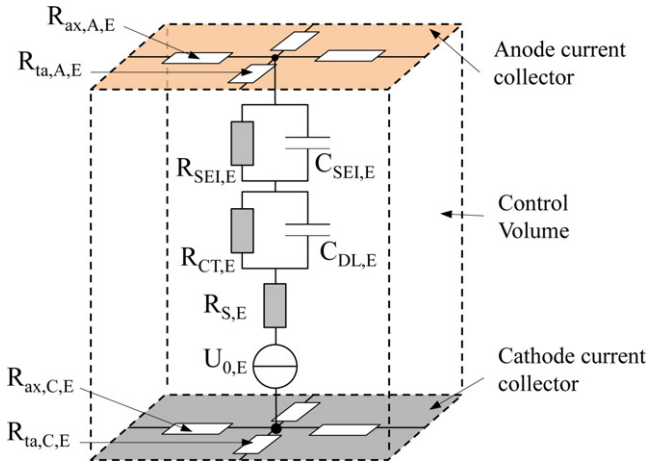

Fig. 5. Section of the used electric FNM-model. Depiction of the ECM of one volume element with its local OCV ($U_{0,E}$) and the ohmic resistances of the anode and cathode current collector to the adjoining volume elements (in axial and tangential direction).

3.2. Electrical model

For the reproduction of the electric cell behavior an equivalent circuit model (ECM) is employed. Buller [20] gives a review on differently complex ECMs used in Li-ion cell simulations. The model chosen for the described investigation consists of a serial resistance in combination with two RC-circuits in series. All elements are parameterized as a function of SoC, temperature and current direction. The values were assumed to be independent from current in the investigated current range. As depicted in Fig. 5 one RC-circuit describes charge transfer resistance (R_{CT}) and double layer capacity (C_{DL}), the other describes the impedance of the solid electrolyte interface (R_{SEI} and C_{SEI}) according to [21]. The serial resistance (R_S) is mainly influenced by the limited conductance of contacts, active materials and electrolyte. Cell inductivity and diffusion overpotentials caused by concentration gradients – often modeled by a Warburg impedance – were neglected. The relatively simple ECM structure is a compromise between accuracy and computing time, as the spatialization of the electric cell model requires multiple solving of the ECM per time step – once for each VE. A method for implementing various components of ECMs in Matlab Simulink for simulation is also given by Buller [20].

As shown in Fig. 5 the described ECM-model of the complete cell was spatialized to an electric Finite-Network-Method (FNM-) model, in which each volume element of the jelly roll (index E in Fig. 5) exhibits its own local anode potential, cathode potential, local impedance, local OCV, local heat generation, and local SoC. For a distinct thermal–electric co-simulation the FNM-model was discretized according to the thermal model. Thus, the nodes on the cathode current collector of each VE are connected to the nodes of the adjoining VEs by pure ohmic resistances in tangential ($R_{ta,C}$) and axial direction ($R_{ax,C}$) calculated by material and geometrical properties. In analogy, this was implemented for the anode nodes ($R_{ta,A}$ and $R_{ax,A}$). The axially outer elements of each radial layer of VE are connected to the accordant terminal by ohmic resistances of the terminal current collectors. These resistances were estimated by geometry and material properties. The electric resistances of anode and cathode current collector, as well as the terminal current collectors, are at least one order of magnitude smaller than the serial resistance of the local ECMs. Thus the estimated ohmic resistances have little impact on the simulation results.

Additionally for every element a linear hysteresis model for determining OCV as a function of SoC, temperature, and load history is integrated – a simplification of the OCV-model of Thele et al. [22].

$$U_{0,E} = \gamma\left(U_{0,ch}(SoC_E) + \frac{dU_{0,ch}}{dT}(T_E - 25\,^\circ C)\right) + (1-\gamma)\left(U_{0,dch}(SoC_E) + \frac{dU_{0,dch}}{dT}(T_E - 25\,^\circ C)\right) \quad (6)$$

The OCV-curves of $U_{0,ch}$ and $U_{0,dch}$ are implemented in 3D look up tables in dependence of SoC and temperature. The coefficient γ describes the linear hysteresis model. It reaches its maximum value of 1 after long charging periods (>5% of SoC) and minimum 0 after long discharging periods (>5% of SoC). Otherwise it decreases linearly with discharge and increases linearly with charge current throughput between 0 and 1 with a gradient of $1/(0.05 \times C_{nom})$.

4. Experimental

Measuring temperature distributions, local current distributions or SoC-gradients inside a jelly roll is not possible in an experimental set-up without disturbing cell configuration and performance. As an indirect evidence of local electric differences, thermal–electric interactions have been validated by observing three cells on different temperature levels electrically connected in parallel. This test was also modeled in thermal–electric cell simulations for validation of the applied model. Object of the investigations were cylindrical $LiFePO_4$ high power cells (specification in Table 1).

Firstly, a cylindrical Li-ion cell with a continuous temperature and current density distribution can simply be modeled as three radially arranged volume elements electrically connected in parallel. The three volume elements exhibiting different temperatures represent the inner, middle and outer region of the cell. Furthermore, each of the three elements is considered in the experiments as single cell (Fig. 6, middle). In order to rebuild temperature gradients between the elements, the three cells connected in parallel were operated at different temperatures. The thermal differences of the three cells during operation were induced by different heat dissipation paths on the cells' surfaces. Cell 1 was radially thermally insulated by a 20 mm thick plastic foam, cell 2 was encased by an insulation of plastic foam as well, but only for half of its length, and cell 3 was exposed to free convection in contact with 5 °C cooled ambient air. The current flow through every cell was measured independently by shunts connected in series to the cells. The three electric paths were routed through a contactor to electrically separate the cells after operating. Different sensors monitored voltage (absolute accuracy: ±5 mV), current (accuracy: ±0.05 A) and housing temperature (accuracy: ±1 K) of every cell.

Fig. 6 (right) shows the schematic diagram of the electric circuit that was connected to a battery test bench. All experiments were executed in a climatic chamber.

Previous to the main experiments (ME 1), the three most similar cells were chosen from a set of six cells by comparing their actual capacity and their internal impedance. The relative differences of measured capacity between the three chosen cells were below 0.5%, the differences of the 10C-pulse impedance below 1%. All measured SoCs in this article are the ratio of the actual usable charge in cell for 1C-discharge current (I_{nom}) at 25 °C and a cutoff voltage of 2 V to the nominal capacity.

$$SoC = \left(\frac{\int_0^{t(U=2V)} I_{nom}\,dt}{C_{nom}}\right)_{T=25\,^\circ C} \quad (7)$$

In order to start the experiment with all three cells at equal states, the cells in the setup were first cooled down by 5 °C ambient temperature and then completely discharged in parallel (cutoff-

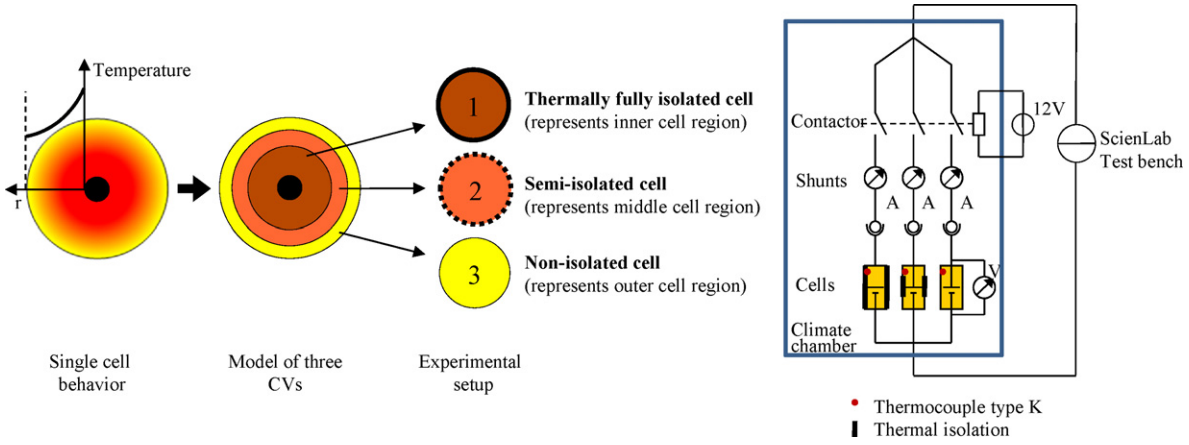

Fig. 6. Experimental approach of three cells at different temperatures electrically connected in parallel; left: transformation of a single cell with continuous temperature distribution to a model with three radial arranged volume elements; middle: representation of the three VEs by the three cells; right: schematic experimental setup with contactor and shunts connected to the battery test bench.

voltage 2 V). Hereupon they were charged with low current (2/3C) to 62% SoC and then rested for 30 m at 5 °C. For an initial warm-up the cells were first heated by 5C pulse cycles (5C for each cell: $3 \times 5C = 66$ A) for 15 m (90 s discharge–90 s charge). Then the current amplitude was increased to $3 \times 8C$ (105.6 A) and the cells were operated for another 2 h. The cells reached a thermal steady state during this period. At the end of the SoC-neutral cycle, the cells were immediately separated by opening the contactors. After tempering the cells to room temperature, their SoCs were separately determined by 1C-discharging to a cutoff-voltage of 2 V.

In a further experiment (ME 2) ME 1 was exactly repeated without separating the cells after cycling. Instead transfer currents during relaxation were enabled and measured for 10 h at 23 °C ambient temperature. This time period was significantly longer than the cooling-down-period of all three cells. Again, SoC-determinations of all cells were performed after separating the cells analog to the previous tests.

For the simulative reproduction of the described experiments the heat transmission coefficients of the cell surfaces to environment were measured by previous experiments as the undefined air flowing conditions in the climate chamber prevent an exact calculation of these values. Therefore the three cells were operated in the experimental setup of ME 1 with SoC-neutral current pulse cycles (90 s discharge–90 s charge) and changing current amplitude, each time until a thermal steady state was reached. The cells' power loss was estimated according to Onda et al. [23]. Considering the difference of cell surface to ambient temperature the heat transfer coefficients were calculated to $\alpha_1 = 15.5$, $\alpha_2 = 23.9$, $\alpha_3 = 40.1$ using Eq. (8).

$$\alpha = \frac{P_{V,avg}}{(T_{s,avg} - T_{amb})A_s} \tag{8}$$

5. Results

The temperature gradient between the three cells of maximal 20 K (fully-isolated to non-isolated) can be seen in Fig. 7. Herein the measured and predicted temperature profiles of the three cells

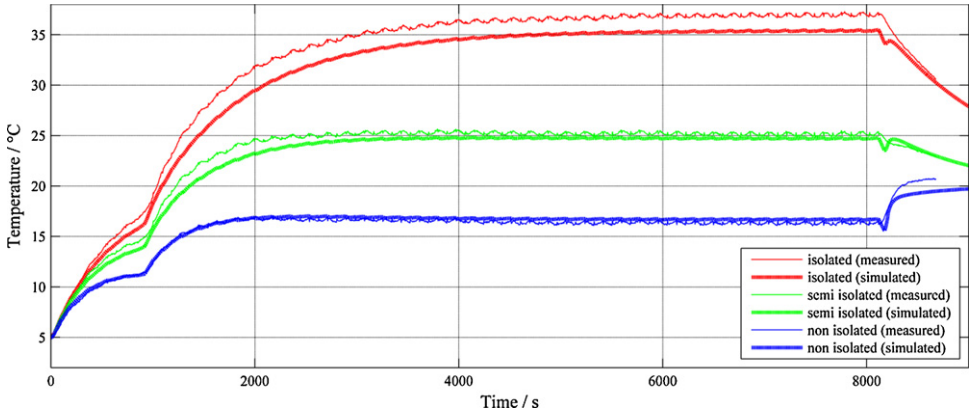

Fig. 7. Temperature development during the pulse cycle of ME1 for the three cells comparing simulated (dashed lines) and measured values (solid lines); blue: non isolated cell, green: semi isolated cell, red: isolated cell. (For interpretation of the references to color in this figure legend, the reader is referred to the web version of the article.)

Table 2
Comparison of measured and simulated average current values for the three cells during the last charge and discharge current pulse at the end of ME 1 (isolated cell: 1, semi-isolated cell: 2, non-isolated cell: 3).

	Average current of last charge pulse $I_{ch,avg}$ (A)		Average current of last discharge pulse $I_{dch,avg}$ (A)	
	Measured	Simulated	Measured	Simulated
Cell 1	40.4	40.1	−40.5	−40.1
Cell 2	34.6	34.6	−34.6	−34.5
Cell 3	30.1	30.1	−30.3	−31.0

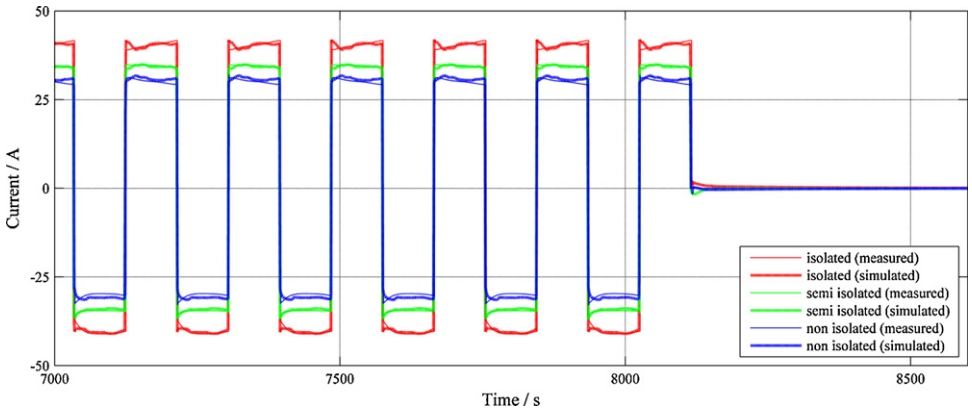

Fig. 8. Current development during the thermal steady of the last cycle pulses of ME 1 for the three cells simulated (dashed lines) and measured values (solid lines); blue: non isolated cell, green: semi isolated cell, red: isolated cell. (For interpretation of the references to color in this figure legend, the reader is referred to the web version of the article.)

on their surfaces are plotted against time. A good agreement of simulation and experimental curves can be seen. The difference of maximal 2 K (occurring for the fully isolated cell) can be explained by the variance of the isolation efficiency between previous and main-experiment.

Caused by growing temperature difference the fraction of current flow through the isolated cell in relation to the entire current is expected to increase, until thermal steady state is reached. The good agreement of simulation and experiment can be seen on the current diagram of the three cells for the last pulses of cycling, where thermal steady state is already reached (Fig. 8). The average currents for the three cells during the last charge ($I_{ch,avg}$) and discharge pulse ($I_{dch,avg}$) are compared in Table 2. The parasitic resistances of the connecting elements and shunts influencing the current distribution were measured to $2.15 \pm 0.04\,m\Omega$ and considered in the simulation.

For the analyzed test the fully isolated cell had – as expected – the lowest SoC right after disconnecting ($SoC_{end,0}$) of the three cells while the non-isolated cell was the highest charged. The values can be seen in Table 3. The impact of OCV hysteresis of the $LiFePO_4$-cell on SoC-behavior during relaxation periods can be illuminated by comparing the results of ME1 and ME2. For the experiment without immediate electric separation (ME 2) we can assume, that the cells' SoCs directly after operation were similar to the values measured for ME1 ($SoC_{end,0}$). The SoC of the cells after the resting period of 10 h ($SoC_{end,\infty}$) were determined by 1C discharge analog to ME1. The difference between $SoC_{end,0}$ and $SoC_{end,\infty}$ for each cell represents its SoC-compensation during relaxation ($\Delta SoC_{transfer}$). To check the values of SoC-compensation the cell currents were recorded and integrated during relaxation period. Both methods of determining $\Delta SoC_{transfer}$ led to similar results.

It can be seen, that during longer rest-periods after high current loads the SoCs of Li-ion cells with hysteresis behavior connected in parallel does not equalize completely. For the investigated operation only about one third of the SoC-difference was equalized during operation both, in the experiment and in simulation. The cells persist stably at differing SoC-values.

6. Discussion

The experimental results in accordance with the simulations detect thermal–electric inhomogeneities between a set of parallel connected $LiFePO_4$-cells of differing temperature. These inhomogeneities have to be expected in non-uniformly cooled battery-packs containing cells connected in parallel. The differences in temperature, current density and SoC lead to inhomogeneous cell aging inside the battery-pack influencing the overall battery performance in the course of time. Although the results may easily be transferred to multi-cell setups, the focus of the following discussion is the quantification of the thermal–electric interactions that are expected inside a single cell.

A $LiFePO_4$-cell – exposed to forced convection – was simulated using the spatialized thermal/electric cell-model. Therefore the ambient temperature of 5 °C and a SoC-neutral pulse-cycle with a magnitude of 70 A were chosen (20 s discharge pulses–20 s charge pulses). The starting SoC was set to 50%. The heat transfer coefficient for an incident flow (lateral to the middle axis) with a velocity of $15\,m\,s^{-1}$ and a cylindrical geometry was calculated to $117.9\,W\,m^2\,K^{-1}$ on cell surface according to [24].

Fig. 9 show snapshots of the respective cell state distributions at the end of the last charge pulse (after 6530 s) in a thermal steady state. All three depictions contain two sectional views, on the left side in the radial–axial plane and on the right side in radial–tangential plane (in the axial middle of the cell).

The simulated temperature distribution in the jelly roll can be seen in Fig. 9a. The maximum temperature of jelly roll is 40.9 °C at the inner part of the jelly roll. The negative temperature gradient increases to the outer regions of the jelly roll. The minimum temperature in the jelly roll for the given scenario is 19.5 °C. Fig. 9b shows the distribution of current flow (between anode and cathode) per volume (current density) with a similar shape as the temperature distribution. It can be seen that the current density in the inner and outer parts of the jelly roll differ by a factor of approx. 1.3, where higher currents are recorded for the inner cell region. The variation of local SoC is monitored in Fig. 9c. For this point in time, where the average cell SoC is equal to the starting SoC, the maximal SoC-difference reaches 9% ($\Delta SoC_{end,0}$).

Fig. 10 shows the SoC profile of the hottest and coldest region inside the jelly roll vs. time. The two exemplary local SoCs disperse induced by rising temperature difference and do not equalize completely after end of cycling according to the influence of OCV-hysteresis ($\Delta SoC_{end,\infty}$ = ca. 5%). According to the simulation a cell that is stored after high current loads would possess a SoC-gradient persisting during rest periods.

In summary the three following spatial thermal–electric effects are expected to influence the aging mechanism and thus the lifetime of $LiFePO_4$-cells as the aging at different jelly roll locations proceeds under different aging condition: generally the impact of temperature on calendar life predictions of Li-ion cells is mostly considered as an exponential dependence (Arrhenius equation) [5,25,26]. Also, an exponential aging behavior vs. temperature is reported in several capacity fading investigations at cycle life conditions [1,5]. For $LiFePO_4$/C-cells the effect of accelerated cycle life aging on elevated temperatures can also be seen in [6]. Assuming

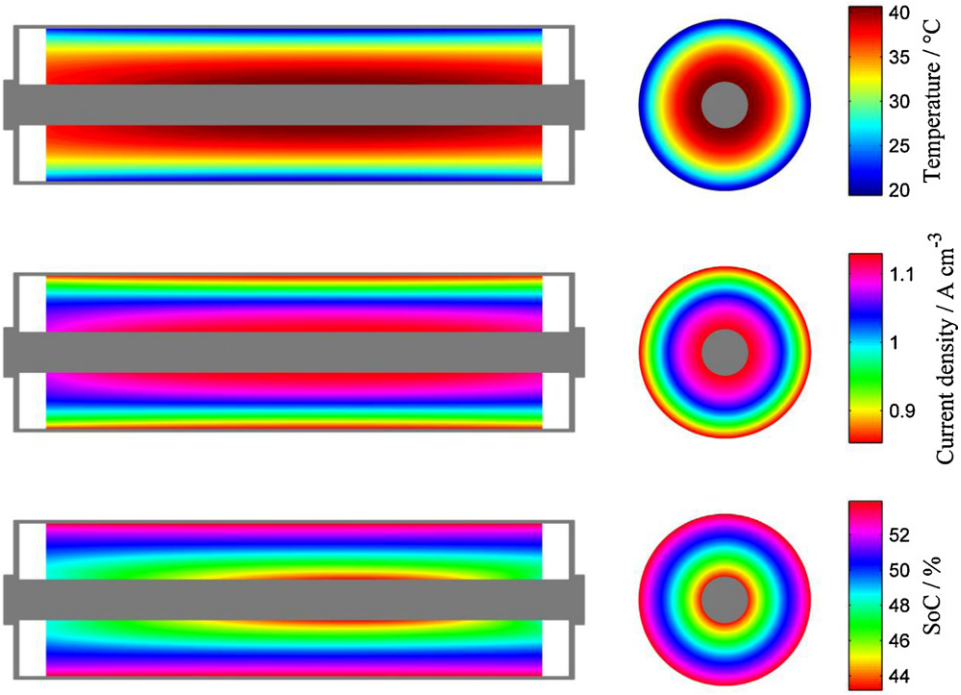

Fig. 9. Simulated temperature distribution (a), current density distribution (b) and SoC-distribution (c) inside the $LiFePO_4$-cell directly at the end of the single cell cycle (t = 6530 s).

an Arrhenius relation, a temperature gradient inside a cell induces an exponentially rising aging behavior of the inner regions of a cylindrical Li-ion cell.

The current distribution caused by the temperature gradient is expected to intensify this unequal aging behavior. E.g. Ning et al. assumes that for $LiCoO_2$-cells capacity fade approx. grows with the square root of the current magnitude [27]. Additionally the increased charge throughput in warmer cell regions is expected to induce locally accelerated capacity fading. According to charge throughput models, which are state of the art for empirical cycle life aging models [28], aging progress is in direct correlation to charge throughput. Thus, a further increased gradient of aging behavior in the interior regions of the cell is expected.

Also thermally induced SoC-distributions can influence the gradient of aging progresses. From other cell chemistries, the SoC-dependence of cell aging is well known. For example Amine et al. [29] showed a significant difference in power fading for a $LiNiCoO_2$/C-cell stored at 40% and 60% SoC at several temperatures. Additionally, faster capacity degradation is expected to occur. However, for $LiFePO_4$/C-systems, which tend to significant SoC-

Table 3
Comparison of cells' SoCs at the end of cycling ($SoC_{end,0}$) and after 10 h resting period ($SoC_{end,\infty}$) in simulation and in experiment. SoC-compensation during relaxation ($\Delta SoC_{transfer}$) is calculated firstly by the difference of $SoC_{end,\infty}$ and $SoC_{end,0}$ and secondly by current integration during relaxation.

	$SoC_{end,0}$		$SoC_{end,\infty}$		$\Delta SoC_{transfer}$	
	Measured (ME 1)	Simulated	Measured (ME 2)	Simulated	Calculated	Current integrated
Cell 1	59.1%	58.9%	60.1%	60.0%	+1.0%	+0.9%
Cell 2	63.1%	63.3%	62.6%	62.7%	−0.6%	−0.4%
Cell 3	64.4%	63.9%	63.7%	63.3%	−0.7%	−0.6%
ΔSoC	−5.3%	−5.0%	−3.6%	−3.3%		

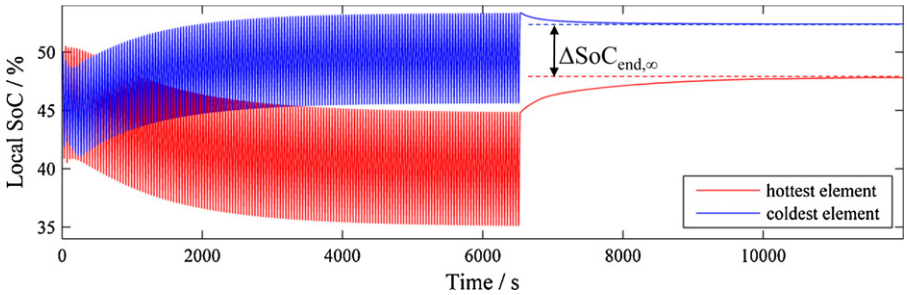

Fig. 10. SoC progress of the hottest (blue line) and coldest cell region (green line) inside the $LiFePO_4$-cell during the single cell cycle with a persisting SoC difference ($\Delta SoC_{end,\infty}$). (For interpretation of the references to color in this figure legend, the reader is referred to the web version of the article.)

Table A1
Abbreviation and parameter definition used in formulas, text and figures.

$Z_p(t)$	Pulse impedance [Ω]	R_S	Serial resistance of the ECM [Ω]
ΔU	Internal voltage drop of cell [V]	R_{CT}	Charge transfer resistance of the ECM [Ω]
ΔI	Current step magnitude [A]	C_{DL}	Double layer capacity of the ECM [F]
U_0	Open circuit voltage [V]	R_{SEI}	Resistance of the solid electrolyte interface in the ECM [Ω]
T	Temperature [K]	C_{SEI}	Capacity of solid electrolyte interface in the ECM [F]
λ	Thermal conductivity [W mK^{-1}]	$R_{ax,C}$	Ohmic resistance of cathode current collector in axial direction between two CV [Ω]
ρ	Density [kg/m^3]	$R_{ta,C}$	Partial resistance of cathode c.c. in tan. direction [Ω]
c	Specific heat capacity [J kg K^{-1}]	$R_{ax,A}$	Partial resistance of anode c.c. in axial direction [Ω]
$\dot{q}_q$	Density of heat source [W m^{-3}]	$R_{ta,A}$	Partial resistance of anode c.c. in tan. direction [Ω]
t	Time [s]	$U_{0,ch}$	OCV after charge load history [V]
r	Radial coordinate	$U_{0,dch}$	OCV after discharge load history [V]
z	Axial coordinate	γ	Linear OCV-hysteresis variable [−]
φ	Tangential coordinate	C_{nom}	Nominal capacity [Ah]
		I_{nom}	Constant discharge current of 4.4A (1C) [A]
Δt	Time step size of simulation [s]	α	Heat transfer coefficient [W (m^{2}K)$^{-1}$]
V_E	Volume of control element [m^3]	$P_{V,avg}$	Average cell power loss [W]
R_{th}	Thermal resistance [K W^{-1}]	T_{amb}	Ambient temperature [K]
$\dot{Q}_{irr}$	Irreversible heat generation [W]	$T_{S,avg}$	Average cell surface temperature [K]
$\dot{Q}_{rev}$	Reversible heat generation [W]	A_S	Cell surface area [m^2]
R_i	ith ohmic resistance of an user-defined equivalent circuit model [Ω]	$I_{ch,avg}$	Average cell current during the last charge pulse (ME 1) [A]
$I_{i,E}$	Current flow through the ith ohmic resistance in the ECM of element E [A]	$I_{dch,avg}$	Average cell current during the last discharge pulse (ME 1) [A]
I_E	Current flow through the serial elements in the ECM of Element E [A]	$SoC_{end,0}$	Cell's SoC at end of cycling
T_{cell}	Temperature of cell [°C]	$SoC_{end,\infty}$	Cell's stable SoC after resting period
I_{cell}	Cell current [A]	$\Delta SoC_{transfer}$	Eliminated SoC difference during relax period.

gradients, the magnitude of SoC-influence on calendar and cycle life aging – and thus on inhomogeneous aging inside a single cell – has to be investigated in future. Furthermore, different electrochemical aging effects that are influenced by high temperature, high cycling rates and high and low SoCs in Li-ion cells are discussed by Vetter et al. [3].

In summary, deduced from literature the three observed inhomogeneities (temperature, current density and SoC) can, in common, lead to a more than linearly accelerated aging progress for the warmer inner regions inside a Li-ion cell compared to the colder outer regions. In consequence, a different and faster aging behavior of the entire cell is expected than for a cell with – hypothetically – absolutely uniform temperature distribution with the same volume averaged temperature. Thus, the consideration of local thermal–electric interactions and the usage of spatially resolved thermal–electric cell models are hence important for aging analysis and therefore for thermal management aspects of Li-ion cells in order to optimize active cooling concepts and strategies.

7. Conclusion

In this article the thermal–electric interactions caused by temperature gradients inside a $LiFePO_4$ cell are treated. In addition to temperature and current gradients a divergence of the local state of charge, the SoC drift, could be explained and verified experimentally even for charge neutral current profiles. The following two effects could be identified as the reasons of the SoC-drift:

1. The temperature dependent ratio of charge to discharge pulse impedance (CDE 1).
2. The temperature dependence of open circuit potential (CDE 2).

Electric inhomogeneities between three differently cooled and electrically in parallel connected $LiFePO_4$-cells were detected both, in experiment and simulation. In the experiments the maximum difference in SoC of 5.3% after a SoC-neutral pulse cycle in a thermal steady state occurred between two cells with a difference in temperature of 20 K. The results of simulation agree well with temperature, current and SoC measurements. Both examinations show that for the given experiment even after long resting periods the SoC-difference between the cells is reduced only to 2/3 of the original value (5.3 → 3.7%). An SoC difference persists due to the OCV-hysteresis, which is significant in $LiFePO_4$/C-cells.

The conclusions for cells connected in parallel were additionally transferred to the single cell behavior. Spatially resolved thermal and electric cell co-simulations of a $LiFePO_4$ cell loaded with a 70 A pulse cycle showed a current density gradient across the jelly roll (i_{inner}/i_{outer}: ca. 1.3) as well as a SoC-incline of 9.5% from inner to outer jelly roll elements caused by a temperature spread from 19.5 °C (outer elements) to 40.9 °C (inner elements). Thus temperature, current and SoC distribution indicates more harsh aging conditions for the warmer parts of a Li-ion cell as well as an accelerated aging of the complete cell in comparison to cells with homogenous temperature distributions. The importance to study the thermal–electrical inhomogeneities for accurate aging examinations can be deduced from the literature. Investigations and experiments considering aging inhomogeneities have to be done both on single cell and on battery pack level.

Appendix A.

See Table A1.

References

[1] I. Bloom, B.W. Cole, J.J. Sohn, S.A. Jones, E.G. Polzin, V.S. Battaglia, G.L. Henriksen, C. Motloch, R. Richardson, T. Unkelhaeuser, D. Ingersoll, H.L. Case, J. Power Sources 101 (2001) 238–247.
[2] E.V. Thomas, H.L. Case, D.H. Doughty, R.G. Jungst, G. Nagasubramanian, E.P. Roth, J. Power Sources 124 (2003) 254–260.
[3] J. Vetter, P. Novák, M.R. Wagner, C. Veit, K.-C. Moeller, J.O. Besenhard, M. Winter, M. Wohlfahrt-Mehrens, C. Vogler, A. Hammouche, J. Power Sources 147 (2005) 269–281.
[4] R.B. Wright, C.G. Motloch, J.R. Belt, J.P. Christophersen, C.D. Ho, R.A. Richardson, I. Bloom, S.A. Jones, V.S. Battaglia, G.L. Henriksen, T. Unkelhaeuser, D. Ingersoll, H.L. Case, S.A. Rogers, R.A. Sutula, J. Power Sources 110 (2002) 445–470.
[5] P. Ramadass, B. Haran, R. White, B.N. Popov, J. Power Sources 123 (2003) 230–240.

[6] P. Liu, J. Wang, J. Hicks-Garner, E. Sherman, S. Soukiazian, M. Verbrugge, H. Tataria, J. Musser, P. Finamore, J. Electrochem. Soc. 157 (2010) A499–A507.
[7] D. Linzen, Impedance-based loss calculation and thermal modeling of electrochemical energy storage devices for design considerations of automotive power systems, PhD Thesis, RWTH Aachen, Shaker Verlag, 2005, ISBN: 3-8322-57006-4.
[8] J. Gerschler, D.U. Sauer, Electric Vehicle Symposium (EVS 24), Stavanger, 2009.
[9] V. Viswanathan, D. Choi, D. Wang, W. Xu, S. Towne, R. Williford, J. Zhang, J. Liu, Z. Yang, J. Power Sources 195 (2010) 3720–3729.
[10] R. Yazami, Y. Reynier, J. Power Sources 153 (2006) 312–318.
[11] Y. Raynier, R. Yazami, B. Fultz, J. Power Sources 119–121 (2003) 850–855.
[12] M. Roscher, D.U. Sauer, J. Power Sources 196 (2011) 331–336.
[13] W.B. Gu, C.Y. Wang, J. Electrochem. Soc. 147 (2000) 2910–2922.
[14] V. Srinivasan, C.Y. Wang, J. Electrochem. Soc. 150 (2003) A98–A106.
[15] MATLAB®, Version 7.5 (R2007b), The MathWorks, Inc., http://www.mathworks.com, Release: 09/2007.
[16] M. Fleckenstein, O. Bohlen, M. Roscher, B. Baeker, 2nd Technical Conference Advanced Battery Technologies for Automobiles, Mainz, 2010.
[17] P. Stephan, Thermodynamik - Einstoffsysteme, Springer Verlag, Heidelberg, 1998.
[18] M.S. Wu, K.H. Liu, Y.Y. Wang, C.C. Wan, J. Power Sources 109 (2002) 160–166.
[19] K.E. Thomas, J. Newman, J. Electrochem. Soc. 150 (2003) A176–A192.
[20] S. Buller, Impedance-based simulation models for energy storage devices in advanced automotive power systems, PhD Thesis, RWTH Aachen, Shaker Verlag, 2002, ISBN: 3-8322-1225-6.
[21] J. Gerschler, J. Kowal, M. Sander, D.U. Sauer, Electric Vehicle Symposium (EVS 22), Yokohama, 2006.
[22] M. Thele, M. Radin-Macukat, D.U. Sauer, O. Bohlen, D. Linzen, E. Karden, Electric Vehicle Symposium (EVS 23), Anaheim, 2007.
[23] K. Onda, H. Kameyama, T. Hanamoto, K. Ito, J. Electrochem. Soc. 150 (2003) A285–A291.
[24] VDI-Waermeatlas, VDI-Gesellschaft, 10th ed., Springer Verlag, Heidelberg, 2006.
[25] E.V. Thomas, I. Bloom, J.P. Christophersen, V.S. Battaglia, J. Power Sources 184 (2008) 312–317.
[26] R.P. Ramasamy, R.E. White, B.N. Popov, J. Power Sources 141 (2005) 298–306.
[27] G. Ning, B. Haran, B.N. Popov, J. Power Sources 117 (2003) 160–169.
[28] D.U. Sauer, H. Wenzl, J. Power Sources 176 (2008) 534–546.
[29] K. Amine, C. Chen, J. Liu, M. Hammond, A. Jansen, D. Dees, I. Bloom, D. Vissers, G. Henriksen, J. Power Sources 97–98 (2001) 684–687.